Bridging the shocked monazite gap – Deformation microstructures in natural and laser shock-loaded samples

Anne-Magali Seydoux-Guillaume, Thibaut de Rességuier, G. Montagnac, S. Reynaud, H. Leroux, B. Reynard, A.J. Cavosie

Bridging the shocked monazite gap- Deformation microstructures in natural and laser shock-loaded samples.

A.-M. Seydoux-Guillaume[1], T. de Resseguier[2], G. Montagnac[3], S. Reynaud[4], H. Leroux[5], B. Reynard[3] and A. J. Cavosie[6].

[1] Univ Lyon, UJM, UCBL, ENSL, CNRS, LGL-TPE, F-42023 Saint Etienne, France

[2] PPRIME, CNRS-ENSMA-Université de Poitiers, 1 avenue Clément Ader, 86961 Futuroscope, France

[3]Univ Lyon, ENSL, UCBL, UJM, CNRS, LGL-TPE, F-69007 Lyon, France

[4] Université de Lyon, UJM-Saint-Etienne, CNRS, Institut d'Optique Graduate School, Laboratoire Hubert Curien UMR 5516, F-42023 Saint-Etienne, France

[5] Univ. Lille, CNRS, INRAE, Centrale Lille, UMR 8207 - UMET - Unité Matériaux et Transformations, F-59000 Lille, France

[6]The Space Science and Technology Centre (SSTC) and the Institute for Geoscience Research (TIGeR), School of Earth and Planetary Science, Curtin University, Perth, WA 6102, Australia

Keywords: Shock metamorphism – Monazite – Laser-shock experiments - Transmission Electron Microscope – Vredefort impact

ABSTRACT

Impact-related damage in minerals and rocks provides key evidence to identify impact structures, and deformation of U-Th-minerals in target rocks, such as monazite, makes possible precise dating and determination of pressure-temperature conditions for impact events. Here a laser-driven shock experiment using a high-energy laser pulse of ns-order duration was carried out on a natural monazite crystal to compare experimentally produced shock-deformation microstructures with those observed in naturally shocked monazite. Deformation microstructures from regions that may have experienced up to ~50 GPa and 1000°C were characterized using Raman spectroscopy and transmission electron

microscopy. Experimental results were compared with nanoscale observations of deformation microstructures found in naturally shocked monazite from the Vredefort impact structure (South Africa). Raman-band broadening observed between unshocked and shocked monazite, responsible for a variation of ~3 cm^{-1} in the FWHM, is interpreted to result from the competition between shock-induced distortion of the lattice, and post-shock annealing. At nanoscale, three main plastic deformation structures were found in both naturally and experimentally shocked monazite: deformation twins, mosaïcism, and deformation bands. The element Ca is enriched along host-twin boundaries, which further confirms that the laser shock loading experiment produced both comparable styles of crystal-plastic deformation, and also localized element mobility, as that found in natural shock-deformed monazite. Deformation twins form in the experiment were only along the (001) plane, an orientation which is not considered diagnostic of shock deformation. However, both mosaïcism and deformation, expressed in SAED patterns as streaking of spots, and the presence of extra spots (more or less pronounced), are interpreted as unambiguous nano-scale signatures of shock metamorphism in monazite. Experimentally calibrated deformation features, such as those documented here at TEM-scale, provide new tools for identifying evidence of shock deformation in natural samples.

1. INTRODUCTION

The formation of meteorite impact craters is a ubiquitous process on planetary surfaces (*French and Koeberl, 2010*). On Earth, few impact craters are accurately and precisely dated due to the lack of suitable age geochronometers (*Schmieder and Kring, 2020*), which makes it difficult to link meteorite impacts to significant events in the geological record (*Jourdan et al., 2012*). As a result, fundamental questions regarding possible links between impact events, changes in the geosphere and biosphere, and the origin of life, all of which rely on the acquisition of both accurate impact conditions and timing, remain debated (*Moser et al., 2019*).

Impact-related damage in minerals and rocks provides key evidence to identify impact structures (*French and Koeberl, 2010*). Shock deformation microstructures have been intensively studied in some minerals, especially quartz, down to the nanometer scale with transmission electron microscopy (TEM), and include formation of dislocations, planar deformation features (PDF), mosaïcism (i.e. a mosaic texture with small domains of crystalline blocks slightly misoriented to each other), twins, high-pressure phases, decomposition, recrystallization, and melting (*e.g., Leroux et al., 1994*). Their formation initially depends on pressure conditions, often above 10 GPa, are attained within nanoseconds to seconds (*Langenhorst and Deutsch, 2012*), and can be modified by subsequent heating. Over the past decade, with the advent of high-spatial resolution techniques, resolving deformation of U-Th-minerals in target rocks (e.g. zircon, monazite, apatite, xenotime, titanite) makes possible precise dating and determination of pressure-temperature conditions (P,T) for impact events. Zircon is the most widely studied geochronometer for shock deformation and forms various shock microstructures (*e.g. Wittmann et al., 2006; Moser et al., 2011; Timms et al. 2017*). In contrast, shocked monazite is less studied; neoblasts (*Erickson et al., 2017; Erickson et al., 2020)*, deformation twins (*Fougerouse et al., 2021a*), and a high-pressure phase (Erickson et al., 2019) can form during shock metamorphism, all of which offer the potential for dating impacts. One important drawback of zircon concerns self-irradiation damage that can lead to complete amorphization (*Ewing et al., 2003*). This has consequences both on the disturbance of the U-Pb geochronological systems (e.g. *Seydoux-Guillaume et al., 2015; Peterman et al., 2016*), and also on formation and retention of deformation microstructures. For example, radiation damage can inhibit the formation of the high-pressure phase reidite (*Lang et al., 2008; Timms et al., 2018*), and obliterate shock microstructures at atom scale over time (*Reimold et al., 2002*). In contrast, despite a much higher radionuclide incorporation rate, monazite is much more resistant to irradiation. Monazite has the ability to remain crystalline over geological time due to self-annealing of radiation damage (*Seydoux-Guillaume et al. 2004; 2018*), and will therefore preserve more or less the same structural state upon impact. In this regard, reliable impact conditions may be more readily extracted from shock-features in monazite.

Published studies show that evidence of impact age resetting in U-Pb geochronometers can be highly heterogeneous due to complex microstructures at the grain scale (*e.g. Cavosie et al., 2018 and 2021*). Shock-deformation in monazite has previously been described (*Schärer and Deutsch, 1990)*, however its microstructure has only been systematically described at the micrometer scale recently using electron backscatter diffraction (EBSD) (*Erickson et al., 2016, 2017, 2020; Cavosie et al., 2018*). No nanometer-scale investigations using TEM to describe shock deformation features in monazite have been conducted previously.

Experimental approaches have been applied to address formation of shock deformation microstructures in monazite (*Deutsch and Schärer, 1990; Huang et al., 2010; Lacomba-Perales et al., 2010; Seydoux-Guillaume et al., 2010; D'Abzac et al., 2012*; *Heuser et al., 2018),* and propose the existence of high-pressure monazite polymorphs which have thus far not been discovered in nature (*Erickson et al., 2019*). Laser-driven experiments have previously demonstrated the ability to simulate conditions of impact events (e.g. in olivine; *Langenhorst et al., 1999*). Here we compare nanoscale deformation structures formed in shocked monazite from the Vredefort impact structure in South Africa (*Cavosie et al., 2018*) with experimentally shocked monazite, in order to identify which features can be used as shock indicators, and also enhance the validity of laser-driven shock-experiments.

2. Materials and Methods

2.1. Starting material

A piece of a centimeter-sized single monazite crystal from Manangotry (Madagascar) was cut in a random orientation, embedded in epoxy and polished (Fig. 1). The sample was previously structurally characterized at the nanoscale by TEM (*Seydoux-Guillaume et al., 2004; Grand'Homme et al., 2018*), particularly with regards to structural defects induced by radiation damage; no twins were observed in previous studies. This monazite crystal is also chemically homogenous, with negligible inclusions and porosity, and has a well-resolved age (555 ± 2 Ma, ID-TIMS; *Paquette and Tiepolo, 2007*).

A shocked monazite grain from the Rietputs Formation in South Africa (Sample Sec-03D, grain 9) was also investigated to evaluate if laser-driven shock experiments are able to reproduce impact damage found in nature. This monazite is a detrital grain that eroded from shocked bedrock at the Vredefort impact structure, and was transported ~500 km downstream in the Vaal River (*Cavosie et al., 2018*). It was previously characterized with BSE and EBSD, and shown to contain an anomalously high density of deformation twins, as well as localized areas that have recrystallized into neoblastic domains (*Cavosie et al., 2018*). The original host rock is unknown, however, it is assumed that the detrital shocked monazite originated from between the 20 and 30 GPa isobars at the Vredefort impact structure, as it is not fully neoblastic (e.g., *Erickson et al., 2017*), and is similar to other detrital shocked monazite grains that host shock-twinned zircon inclusions (*Erickson et al., 2016*).

2.2. Laser-driven shock loading

The laser shock experiment was carried out at the "nano2000" facility of the *Laboratoire pour l'Utilisation des Lasers Intenses* (LULI, UMR CNRS 7605, Ecole Polytechnique, Palaiseau, France). The target consisted of a 20 µm-thick Al foil glued on top of the monazite crystal (Fig. 1a). A high-power laser pulse of 1.06 µm-wavelength, 5 ns-duration, 765 J-energy, was focused onto a 3.2 mm-diameter spot on the target surface. The resulting laser intensity was about 1.9×10^{12} W/cm². A thin absorbing layer of Al (~µm-order) is ablated into a plasma cloud, whose expansion drives a short compressive pulse. The amplitude (50 GPa) of this pressure pulse and its temporal shape (about 6 ns-duration at half maximum) were inferred from a simulation of laser-matter interaction, using the measured profile of laser intensity as an input boundary condition. Shock pressure transmitted to the monazite sample across the Al-monazite interface was estimated by accounting for the impedance mismatch between both materials, using data reported for $CePO_4$ monazite (*Feng et al., 2013; Du et al. 2009*). Peak loading pressure applied on the monazite crystal was thus calculated at 56.7 GPa. The post-shock temperature computed in Al is about 1300 K, which agrees with calculated thermodynamic data for a 50 GPa mean

shock pressure (*Kinslow, 1970*). The subsequent post-release temperature in Al after pressure unloading is about 700 K. In the monazite crystal however, shock-induced heating cannot be assessed without an equation of state for this material, but it should be similar in a natural impact event for an analogous loading pressure, as temperature only depends on shock pressure. Nevertheless, the much shorter during of both pressure and temperature under laser-driven compression may result in differences in shock-induced transformations, due to (i) possible kinetic inhibition of time-consuming processes (e.g. diffusion, conduction), and (ii) faster pressure decay with propagation distance which would strongly restrict the size of the shock-heated region and possibly hinder neighbourhood effects within heterogeneous samples. One goal of this study is thus to address both relevance and limitations of the impact/laser analog.

2.3. Analytical methods.

Raman spectra were collected directly on the shocked surface of the monazite crystal in clean areas (Fig. 1d-g) with a Horiba micro-Raman spectrometer LabRam HR800 evolution. Groups of 10 spectra were collected respectively on starting material, shocked samples C1 and C2, with two accumulations of 10 s exposure (Fig. 2a). Raman peaks were fitted with Gauss-Lorentz spectral models in the spectral range from 800 to 1200 cm^{-1}, with the Matlab application tool PeakFit to extract the position and full width at half maximum (FWHM) of the v_1 peak (Fig. 2b, Table S1). FWHM values are corrected for the apparatus function of the Raman instrument (*Nasdala et al., 2001*).

The TEM foils were prepared using a Thermo Fisher Scientific FEI 125 Helios Nanolab 600i focused-ion beam scanning electron microscope (FIB/SEM) hosted by MANUTECH USD platform, at Hubert Curien laboratory, Saint-Etienne (France). Nanoscale characterization was performed with a Cs-corrected TEM (NeoARM200F Cold FEG) at 200 kV, operated by the CLYM and hosted within the Hubert Curien Laboratory, Saint-Etienne (France). A Gaussian low-pass filter for noise reduction was applied to high-magnification STEM images (Figures 5d-f, 7a-c and 8g and i).

153 For further details see Supplementary Materials.

154

155 **3. RESULTS**

156 *3.1. Optical and SEM observations*

157 After the shock experiment the Al-foil was removed but some glue remained on the surface
158 (dark areas in Figure 1d and also SEM images in figures 1f and g, rough zones on the surface). Only
159 domains free of glue were targeted for analysis (Raman and TEM), i.e. zones C1 and C2. In optical light
160 the central zone is a rounded area where the shock was most intense (Fig. 1b-d); it is approximately 3
161 mm in diameter, which matches the 3.2 mm-diameter of the irradiated spot in the Al foil (Fig. 1b).
162 Numerous planar fractures in monazite are visible in this area, with at least two directions nearly
163 perpendicular to each other (arrows in Fig. 1 c-g). Some of the planar microstructures appear open
164 (Fig. 1c and g), and thus may be tensile fractures.

165

166 *3.2. Raman observations*

167 Raman measurements were performed on both unshocked areas of the monazite crystal and
168 in the central shocked zone (C1 and C2; Fig. 1). The first result is that only monazite was identified; no
169 peaks associated with other phases were present. As described in *Heuser et al. (2018),* bands between
170 900 and 1100 cm^{-1} can be assigned to antisymmetric (ν_3) and symmetric (ν_1) stretching modes,
171 respectively, and peaks between 400 and 700 cm^{-1} to antisymmetric (ν_4) and symmetric (ν_2) bending
172 modes of the PO_4 group of monazite. Differences between the three areas are apparent only in the
173 position and shape of the peaks. As previously shown (*Seydoux-Guillaume et al., 2002; Ruschel et al.,*
174 *2012*) the FWHM of the ν_1 Raman band is suitable to estimate the degree of short-range order of
175 monazite (Fig. 2b). Mean values for the position vary from 969.40 cm^{-1} for unshocked monazite to
176 968.81 and 968.34 cm^{-1} for shocked monazite (C1 and C2 zones respectively), and for FWHM from
177 18.34 (unshocked monazite) to 21.52 and 21.45 cm^{-1} (C1 and C2 respectively). The positions and
178 FWHM are more variable in shocked areas (968.62-968.93/21.20-21.94 cm^{-1} for C1, 968.13-

968.57/21.09-21.93 cm^{-1} for C2) than unshocked areas (969.30-969.51/18.10-18.73 cm^{-1}) of the crystal, indicating a higher local variability of microstructure.

3.3. Transmission Electron Microscopy

Nanoscale characterization was conducted on two TEM foils extracted from the central part of the shocked monazite sample: one in area C1 (FIB1), and one in area C2 (FIB5), a little further from the center of the shocked zone (Fig. 1). Both foils allow observations to be made over approximately 8 µm of depth, from the surface to the interior of the monazite crystal. In the following sections (3.3.1 and 3.3.2) different deformation structures induced by laser-driven shock loading are described. Two TEM foils were also prepared from the naturally shocked monazite grain from Vredefort for comparison (Fig. 8), and deformation structures are described in section 3.3.3.

Each monazite sample reveals typical contrasts in bright-field (BF) TEM mode due to radiation damage (*Seydoux-Guillaume et al., 2004*). The starting (i.e. unshocked) monazite sample as well shows typical mottled diffraction contrasts due to the presence of a distorted lattice (*Seydoux-Guillaume et al., 2002*). The diffraction contrasts are a consequence of the competition between defect formation and annealing of radiation damage (*Seydoux-Guillaume et al., 2018*). However, the distortion is not sufficient to induce visible stretching of diffraction spots (see *Seydoux-Guillaume et al., 2004*), and therefore implies an absence of mosaïcism.

3.3.1. TEM foil C2 (FIB5) – Figures 3 to 5

In this sample two kinds of deformation features were observed, depending on depth of observation within the foil. From the surface down to approximately 4 µm (Fig. 3a), the sample revealed a high density of 10-20 nm domains that are slightly misoriented with respect to each other, resulting in mottled diffraction contrasts in BF-TEM (Fig. 3a-b). Selected area electron diffraction patterns (SAED) show a slight stretching of diffraction spots (Fig. 3c and e), indicative of a small misorientation of domains (<2 degrees). When the crystal is oriented parallel to the [100] zone axis,

205 the most intense stretching is seen along the (012) plane. Additional diffuse spots are also visible
206 (arrows in Fig. 3e) and are measured at a distance of 3.16 Å, compatible with the monazite structure.
207 At higher magnification moiré fringes (arrows in Fig. 3d) are observed and provide further evidence of
208 misorientation of the nano-domains. From 4 µm depth to the bottom of the foil (Fig. 4a), the structure
209 is dominated by bands subparallel to the shock-loaded surface (Fig. 4b). The bands are 300 ± 50 nm
210 long and about 50 nm wide, are relatively regular, and form a wavy pattern within the sample (Fig. 4
211 c-d). Contrast within the bands is homogeneous, with a grey color, and almost no Bragg contrast,
212 consistent with a low crystallinity, almost glassy structure. An SAED pattern parallel to the [100] zone
213 axis that overlaps a deformation band and the adjacent monazite confirms the presence of a diffuse
214 ring, characteristic of amorphous material that is superimposed on the monazite diffraction signature.
215 The same SAED pattern also revealed the appearance of additional spots, some close to the principal
216 spots from the [100] zone axis (Fig. 4e). The most visible additional spots in the SAED pattern, with the
217 shortest distance, are indicated by arrows in Figure 4e, and correspond to a d_{hkl} of 3.58 Å, close to the
218 distance measured in the part of foil closer to the polished surface (Fig. 3e). Additional spots at 2.59,
219 2.17, 2.01, 1.80 Å are all compatible with the monazite lattice. The same region was observed using
220 scanning TEM (STEM) with an annular dark field (ADF) detector (Fig. 5). In this mode, Bragg contrasts
221 are strongly reduced and contrast arises from atomic number and density. The bands appear darker
222 (Fig. 5a-e) due to the lower density of the glassy material within the deformation band (Fig. 5a-b). At
223 very high magnification (Fig. 5e-f) the atomic arrangement within the monazite structure is revealed.
224 In ADF mode, only the heaviest atoms are visible (i.e. rare earth elements like Ce in $CePO_4$ monazite
225 structure); in Figure 5f the pattern matches the arrangement of Ce atoms in monazite along the [100]
226 direction. High resolution STEM imaging and associated Fast Fourier Transform (FFT; Fig. 5c-e) show
227 that the deformation bands are not completely amorphous, and contain highly disoriented nano-
228 crystals of monazite; in Figures 5d and 5e some fringes can be observed within these bands. FFT of
229 different areas in Figure 5c show the strong disorientation from the [100] direction (FFT1) depending
230 on position in the band (compare FFT2 and 3 in Fig. 5c). In FFT3 the area is strongly disoriented with

231 only a faint (0-11) reflection visible. Extra spots observed at 3.58 Å in SAED in TEM mode (Fig. 4e) are
232 also visible (arrows in FFT2), and appear when crossing the band (see arrows in FFT2).
233
234 *3.3.2. TEM foil C1 (FIB1) – Figures 6 and 7 (and Supplementary Data S2; Figures S7)*
235 The TEM foil in area C1 displays twins over the entire foil. In BF-TEM many twin boundaries
236 can be observed at low resolution (Fig. 6a), all parallel to each other. The twins are relatively thick
237 (280 nm to 1.4 µm), with only one direction oriented about 70° from the surface plane. One fracture
238 propagated from the surface into the crystal parallel to the twin boundaries. The twins are oriented
239 parallel to (001), as indicated in the SAED pattern (Fig. 6g) collected across two twin boundaries shown
240 in Figure 6d. Tilting the sample highlighted the twin boundaries and the mottled Bragg diffraction
241 contrasts resulting from radiation damage (Fig. 6b and c). The contrasts are not as pronounced as
242 those in area C2 (Fig. 3 and 4), which agrees with the absence of streaking of SAED spots or the
243 presence of extra spots (Fig. 6e and g). These contrasts are similar to those found in the same
244 unshocked monazite crystal (see Fig. 3c in *Seydoux-Guillaume et al., 2004* and figures 7 to 10 in
245 *Grand'homme et al., 2018*). One twin was imaged in dark field mode (Fig. 6f) collected with the (11-1)
246 plane (Fig. 6g). Further observations in STEM mode (Fig. 7) were made with the monazite crystal
247 oriented along the [110] zone axis, as shown in the SAED pattern in Figure 6e (area shown in Fig. 6a).
248 One twin boundary is observed at high resolution in ADF (Fig. 7a) and annular BF (ABF) (Fig. 7a) mode.
249 In ADF only heavy atoms are visible whereas in ABF lighter atoms can be observed (mostly P). A high
250 magnification image in ADF mode illustrates the match between the arrangement of the Ce atoms
251 along the [110] direction (Fig. 7c) with the expected crystalline pattern. Energy dispersive
252 spectrometry (EDS) chemical mapping across the twin boundary revealed an enrichment in Ca within
253 the twin boundary (Fig. 7d and Supplementary data S7a); in contrast no enrichment nor depletion of
254 Pb was observed within the boundary (Figure S7b in Supplementary data).
255

3.3.3. TEM foils of naturally shocked Vredefort monazite – Figure 8 (and Supplementary Data S2; Figures S8)

Two FIB-foils were prepared from different areas of Vredefort monazite Sec-03D, grain 9 (*Cavosie et al., 2018*). One is located across deformation twins; the other is located a few micrometers away from the first one, outside the twin, and did not cross a twin boundary (Figure S8a in Supplementary data). Three kinds of deformation features were observed in the Vredefort grain: the first TEM-foil contains deformation twins (Fig. 8a, d, g and h), and the second foil contains mosaïcism (Fig. 8b and e) and deformation bands (Fig. 8c and f). Some twins are visible along the (001) plane (Fig. 8a). The (001) deformation twins are consistent with those reported from prior EBSD analysis (*Cavosie et al., 2018*); other orientations of twins present within the sample were not encountered in the experimental sample. Twins along the (001) plane range from 250 nm to 1.1 µm in width, and contain an enrichment in Ca along the twin-host boundary but no enrichment nor depletion of Pb (Fig. 8h and S8b in Supplementary data). In the second TEM-foil (Fig. 8b, e, c, f, i), mosaïcism was observed, with the presence of nano-domains (~20 nm) slightly misoriented with respect to each other, and a slight stretching of diffraction spots, indicative of a small misorientation (<2 degrees) of the domains (Fig. 8b and e). Additional diffuse spots (arrows in Fig. 8e) are measured at a distance of 3.25 Å, compatible with the monazite structure. Deeper within the foil, the structure is dominated by deformation bands (~300 nm long), in which almost no Bragg contrast is visible. The most visible additional spots in the SAED pattern (arrow in Fig. 8f) that overlaps a deformation band and the adjacent monazite, correspond to a d_{hkl} of 3.26 Å. High resolution ADF-STEM imaging (Fig. 8i) show that the deformation band is not completely amorphous (see fringes in the upper part of the image 8i).

4. Discussion

4.1. Experimental shock-deformation features up to the nanoscale.

Early shock experiments on monazite (up to 59 GPa) used the shock-wave reverberation technique and high explosives for planar shock-wave generation (*Deutsch and Schärer, 1990)*; the

shocked monazite grains exhibited lower birefringence, decolorization, intense mosaicism and the presence of fractures. Laser shock experiments on monazite by femtosecond laser ablation show the effect of high-pressure shock waves caused by plasma expansion, revealing nanostructural deformation features below the ablation crater, including fractures, mosaïcism, and deformation twins (*Seydoux-Guillaume et al., 2010; D'Abzac et al., 2012*). Static experimental data (using diamond anvil cell) focused on high-pressure transformation of monazite with various compositions ($CePO_4$-*Huang et al., 2010*; $SmTbPO_4$-*Heuser et al., 2018;* La, Nd, Eu, $GdPO_4$-*Lacomba-Perales et al., 2010*). *Huang et al. (2010)* revealed only structural lattice distortion at around 11 GPa, with no phase transition up to 20 GPa. In contrast, *Lacomba-Perales et al. (2010)* identified a non-reversible high-pressure phase with barite-type structure at 26 GPa for $LaPO_4$ but no phase transition up to 30 GPa for other compositions (Gd, Eu, $NdPO_4$).

In the present study, no significant difference between Raman spectra was observed between unshocked and shocked monazite samples, except for the structural distortion responsible for both Raman-band broadening and data spreading; hence no evidence for formation of a high-pressure phase was found (Fig. 2). Raman-band broadening of natural monazite is due to the combination of two effects: chemical composition (mostly Th, U, Ca and Pb) and lattice distortion caused by radiation damage *(e.g. Nasdala et al., 2002; Seydoux-Guillaume et al., 2002; Ruschel et al., 2012). Ruschel et al. (2012)* proposed an empirical formula for estimating the degree of radiation damage if the chemical composition is known:

$$\text{FWHM } [\text{cm}^{-1}] = 3{,}95 + 26{,}66 \times (\text{Th+U+Ca+Pb}) \text{ [apfu]}$$

where FWHM is the full width at half maximum of the most intense Raman band of monazite (i.e., the ν_1 symmetric PO_4 stretching mode near 970 cm^{-1}; Fig. 2). The monazite used for our experiments contains 0.12, 0.002, 0.045, and 0.003 apfu (based on 4O) for Th, U, Ca and Pb respectively, which gives a ∑(Th+U+Ca+Pb) of 0.17 apfu (*Seydoux-Guillaume et al., 2004*). The expected FWHM is then 8.5 cm^{-1} for monazite with the same composition and no radiation damage. The FWHM of the unshocked monazite is 18.3 cm^{-1}. Interestingly, the monazite used in the present study corresponds closely to the

F6 monazite described in *Ruschel et al. (2012)*, with a ∑(Th+U+Ca+Pb) of 0.15, a $FWHM_{unannealed}$ of 18.1 cm^{-1} and a $FWHM_{annealed}$ of 7.9 cm^{-1}. The difference in width of Raman peaks between $FWHM_{unannealed/unshocked}$ (18.1 and 18.3 cm^{-1}) values to $FWHM_{annealed}$ (7.9 and 8.5 cm^{-1}) values is attributed to the "radiation damage component" (~10 cm^{-1}). The FWHM of Raman-bands from the shocked monazite domains C1 and C2 are ~21.5 cm^{-1} (Fig. 2). The ~3 cm^{-1} difference in the FWHM of the Raman band between the unshocked and shocked monazite is attributed to shock-induced distortion of the lattice. The FWHM increase is expected when grain size is reduced, as broadening is inversely proportional to grain size in CeO_2 ceramics (e.g., *Gouadec and Colomban, 2007*). In ceria, band broadening of 3 cm^{-1} is observed for grain size of about 40 nm, thus the observed broadening of 3 cm^{-1} is consistent with the TEM observation of mosaicism at a similar scale (Fig. 3).

Raman band broadening is essentially related to two nano-features identified using TEM: mosaicism (Fig. 3) and the presence of planar band structures (Fig. 4). As the unshocked monazite crystal already contains radiation damage, expressed as typical mottled diffraction contrasts in BF-TEM mode (Fig. 6a-c) and corresponding to small lattice distortion and the presence of strain (*Seydoux-Guillaume et al., 2002; 2004; 2018*), it is not obvious how to isolate the "radiation damage component" from the "shock component", as done in the previous paragraph with Raman. The role of radiation damage, and therefore the role of "initial structural state" of monazite at time of impact, and formation of shock-deformation features, is discussed below. As the unshocked monazite was previously well-characterized, it is here possible to distinguish some of the shock effects. Note especially BF-TEM images in *Grand'homme et al. (2018),* Figures 7, 9 and 10 (Mnz1). Mosaicism was absent in the pristine monazite crystal (*Seydoux-Guillaume et al., 2004*). Obvious streaking in the diffraction spots (Fig. 3c), moiré fringes (Fig. 3d), and the presence of extra diffraction spots in the SAED pattern (Fig. 3e), are all evidence that the monazite nanodomains are misorientated by a few degrees, i.e. mosaicism.

The deformation bands (Fig. 4) have not been observed in monazite before, even in shocked samples from femtosecond-laser experiments (*Seydoux-Guillaume et al.,2010*; *d'Abzac et al. 2012)*;

this microstructure unambiguously formed in response to the shock experiment. The orientation of the deformation bands is parallel to the direction of shock wave propagation into the crystal (Fig. 4a-b). They are different from typical planar deformation features (PDF) classically observed in shocked silicates like quartz (*Langenhorst and Deutsch, 2012*) or zircon (*Reimold et al., 2002; Leroux et al., 1999*), which are straight, sharp and continuous planes, filled with amorphous material, and sometimes decorated by bubbles formed during post-shock processes, such as annealing or alteration (*Langenhorst and Deutsch, 2012).* In the present shocked monazite, the band structures are shorter (hundreds of nm long) and are not filled with an entirely amorphous material but instead are defined by nanometer sized domains with a highly different orientation, as shown in STEM-ADF images (Fig. 5c-e and in the various FFT from Fig. 5c). This observation is also confirmed by the presence of diffraction contrasts in BF-TEM (Fig. 4c-d), a SAED pattern which shows almost no diffuse diffraction ring (Fig. 4e) but instead contains extra spots characteristic of a monazite lattice, and streaking of spots corresponding to high misorientation of nanodomains to each other and from orientation of the monazite host. We suggest that such features may represent precursor microstructural damage that leads to formation of more typical features found in shocked monazite, such as planar deformation bands (e.g. *Erickson et al., 2016)*. Another possibility is that they represent partly annealed PDFs, similar to those described in various shocked minerals (e.g. *Leroux et al., 2001*), which do not remain amorphous after shock due to the ability of monazite to recrystallize in response to thermal and/or ionization processes (*Seydoux-Guillaume et al., 2004 and 2018*). These highly misoriented deformation band structures could also represent domains from which either neoblasts or high-pressure phase crystallize. Additional diffraction spots observed within these domains can all be attributed to the monazite lattice (Figs. 4d-e and 8 c and f), and thus might also represent incipient formation of neoblasts.

Mechanical twins, formed in response to plastic deformation, are commonly observed in shocked monazite from nature (*Cavosie et al., 2018; Erickson et al., 2017, 2019; Fougerouse et al., 2021a*) and in experiments (*Seydoux-Guillaume et al., 2010*). However, twins in (100), (001) and (120),

are commonly formed during deformation, including indentation experiments (*Hay and Marshall, 2003*) and tectonically deformed monazite (*Erickson et al., 2015; Fougerouse et al., 2021b*). Such twin orientations therefore cannot be used as diagnostic evidence to identify a shock event (see *Erickson et al., 2016*). In the present study (Fig. 6), only twins in (001) were formed in the experimentally shocked monazite; these are obtained with a glide plane at the interface, with displacement vector $\frac{1}{2}$[010], and are exactly the same configuration as that found in indentation experiments (*Hay and Marshall, 2003*). Such twins were not present in the original crystal and were not detected outside the shocked region. Considering the mottled diffraction contrasts revealed in BF-TEM mode (Fig. 6b-c), they are very different from those observed in the other FIB-foil (Figs. 3 and 4) but are very similar to the typical Bragg contrasts commonly observed in natural monazite samples, and correspond to radiation damage (*Seydoux-Guillaume et al., 2002; 2018*). Therefore, in the area of C1, energy involved during the shock event was used to form twins and not highly disoriented domains, as in area C2. Such a contrasting response might be due to possible differences in the loading conditions, with some edge effects (lateral release, shear deformation) at the periphery (area C2) vs. uniaxial strain under planar shock propagation in the central region (area C1). However, further observations are needed to address the distribution of deformation twins in the experimental sample. Furthermore, either the temperature was too low to completely heal defects (< 900°C; *Seydoux-Guillaume et al., 2002*), or the kinetics of the shock experiment were too fast (few nanoseconds duration) to allow complete healing of the monazite lattice.

Finally, an interesting observation here concerns the enrichment in Ca within the twin boundary (Fig. 7d and S7a and b). Segregation of Ca during such a very short (ns) process is difficult to attribute to volume diffusion, which is slow in monazite; it takes 25 s for Ca to diffuse 1 nm at 1300 °C and 48 h at 1000 °C (*Gardès et al., 2007*). Diffusivities used for these calculations were obtained from Pb⇔ Ca interdiffusion experiments, and are controlled by the slower species, in this case Pb. Here, the mobility of Ca during the shock experiment may be enhanced by the presence of dislocations formed in response to the shock, and could explain its enrichment over ~2 nm along a twin boundary.

In natural monazite crystals (e.g. *Seydoux-Guillaume et al., 2003; 2019; Fougerouse et al., 2018; 2021a and b*), Ca-Pb-rich nanoclusters are often found in old (>1 Ga) samples, and may explain the segregation of Ca along twin boundaries or dislocations during a deformation event; however, the monazite crystal used in the present study is relatively young (550 Ma) and nanoclusters were not observed. Monazite forms chains along [001] of alternating phosphate tetrahedra and REE polyhedra (9-fold coordinated). In the monazite lattice, Ca has no "structural" position; it is only incorporated by exchange of $2REE^{3+}$ for Ca^{2+} + $(Th, U)^{4+}$ as cheralite substitution in the REE polyhedra. Furthermore, as REE-O bonds are more likely to break than P-O bonds during twinning (*Hay and Marshall, 2003*), this would first affect the Ca-O bonds and potentially expel Ca along the twin boundary during its formation. This idea was suggested by *Fougerouse et al. (2021b)*, in a 1700 Ma old tectonically deformed monazite, where Ca is also enriched along the twin boundary.

4.2. Laser-shock experiments as analogues for naturally-shocked samples

One of the main objectives of the present study is to evaluate if laser-driven shock experiments reproduce the types of impact damage previously characterized in naturally shocked monazite. Shocked monazite has been reported both in bedrock of the Vredefort impact structure, South Africa (*Moser, 1997, Erickson et al., 2017*), the Nördlinger Ries crater, Germany, the Haughton dome, Canada (*Erickson et al., 2019*), the Araguainha crater, Brazil (*Erickson et al., 2017*), the Woodleigh impact structure in Australia (*Fougerouse et al., 2021a*), the Yarrabubba monzogranite and Barlangi granophyre impact melt (*Erickson et al., 2020*), and in both modern and Pleistocene alluvial deposits of the Vaal River in South Africa as detrital grains (*Cavosie et al., 2010; Erickson et al., 2013; Cavosie et al., 2018*). *Erickson et al. (2019)* reported shocked monazite grains from Ries Crater and Haughton dome with complex yet systematic twin relations produced by reversion from an unquenchable high-pressure tetragonal polymorph, a phase not previously known. No studies have investigated shock-deformation structures in monazite at a nanometer scale, except a recent study by *Fougerouse et al. (2021a)* that focused on Pb mobility as determined from atom probe tomography, a

method shown previously to demonstrate atom-scale element mobility or segregation on twin boundaries triggered by tectonic deformation (*Fougerouse et al., 2021b*).

Several features observed in the naturally shocked Vredefort monazite analyzed here (Fig. 8) correspond in many aspects to features in our laser-driven experiments (Figs. 3-4), including (a) the streaking of spots, (b) the presence of extra spots in SAED patterns (indicated by arrows in Fig. 8) with d_{hkl} possibly attributed to monazite lattice (3.25 Å and 3.26 Å in Fig. 8e and f respectively), (c) deformation twins formed along the (001) plane with enrichment in Ca along the twin-host boundary, (d) mosaïcism, and above all (e) the highly disoriented bands. Comparisons between both samples are easily done, as the reference frame (zone axis) for both sets of observations is exactly the same. The striking similarity shows that the different features observed beneath the laser shock-loaded surface cannot be attributed to possible artefacts of the laser experiment (e.g. annealing upon conductive heating from the Al plasma, or spreading of the compression front upon transmission through the thin glue layer), as the same features are found in naturally shocked monazite.

These results demonstrate the ability of laser-driven experiments to produce shock deformation microstructures found in naturally shocked monazite, specifically mosaïcism, twinning and deformation bands. One additional microstructure described by *Cavosie et al. (2018) and Erickson et al. (2017)* is the formation of neoblastic domains, which were not observed in the experimental products. The presence of neoblastic domains provides evidence of localized recrystallisation of monazite during, or more likely, immediately following shock deformation. The absence of neoblasts in the laser shock-loaded monazite crystal may be explained by either (i) lower shock conditions (essentially temperature), too low to induce recrystallization, in contrast to what can be observed in naturally shocked monazite (e.g. *Erickson et al., 2017; 2020*), or by (ii) insufficient duration of the thermomechanical load, shorter by many orders of magnitude in the experiment (~6 ns-pressure pulse, see Section 2.2), which may be below the characteristic time required to form neoblasts.

Finally, the fact that in both cases Ca is significantly enriched within host-twin boundaries over a few nm (compare figures 7d and 8h and S7a-b and S8b), which has been reported previously in

438 shocked monazite (see Ca segregation in Figure 5a of *Fougerouse et al., 2021a*) further confirms that
439 laser shock loading produced both comparable styles of crystal-plastic deformation, and also localized
440 element mobility, thus reproducing shock microstructures found in nature. Even if the mechanism of
441 Ca-segregation is not completely understood, shock conditions of our laser-driven experiments seem
442 sufficient to induce atomic segregation during twin formation. Future studies will evaluate the
443 mobility mechanism and the ability of such experiments to reset geochronological systems by
444 liberating Pb from the structure during twin formation, as suggested by *Fougerouse et al. (2021a)* for
445 shock twins and also in tectonically deformed monazite samples by *Fougerouse et al. (2021b)*. In this
446 study, however, no segregation of Pb was observed in the investigated TEM foils (See Supplementary
447 Data S2; Figures S7b).
448
449 *4.3. Role of radiation damage in formation of shock-deformation features?*
450 In order to ascertain shock conditions of minerals during impact events, the structural state
451 of the mineral at the time of impact must be estimated. In the case of zircon, a mineral highly sensitive
452 to radiation damage, formation of the high-pressure polymorph reidite is inhibited in partially
453 metamict zircon due to the general reduction in longitudinal and shear stiffness with radiation damage
454 (*Erickson et al., 2017; Timms et al., 2018*). Extrapolation of impact conditions in natural shocked zircon
455 can thus be complicated due to lack of knowledge of pre-impact intrinsic properties. In contrast,
456 monazite has the ability to remain crystalline over geological time due to self-annealing of radiation
457 damage (*Seydoux-Guillaume et al. 2004; 2018b*), however it is not known if the presence of radiation
458 damage influences formation of shock-deformation features or high-pressure polymorphs (e.g.,
459 *Erickson et al., 2019*). Further shock-experiments using monazite free of radiation damage as a starting
460 material may be able to elucidate such behavior.
461 It is also worth considering that monazite samples older than 1 Ga may have accumulated a
462 high amount of radiogenic Pb in the lattice and received intensive radiation doses. Even if clear
463 evidence for radiation damage is limited to nm-isolated domains within monazite resulting in lattice

distortion (*Seydoux-Guillaume et al., 2004*), these effects induce Raman broadening and mottled diffraction contrasts visible in TEM. At the micrometer scale, peak broadening of Raman spectra provides one indication that monazite crystals were affected by a shock event. This requires, however, knowledge of both composition and FWHM of Raman spectra of unshocked monazite samples, in order to evaluate the radiation damage component, which produces the same broadening effect (*Nasdala et al., 2002; Seydoux-Guillaume et al., 2002; Ruschel et al., 2012*). More investigations using TEM are needed to confirm a primary (shock) interpretation, and to describe in detail shock deformation features. Analysis of shocked monazite by TEM, away from twinned domains (Figs. 3 to 5), revealed intense lattice distortion in the form of mosaicism, deformation bands, and the presence of intense streaking and extra spots in the SAED pattern; these features can unambiguously be attributed to shock deformation. Unshocked monazite crystals (e.g. *Seydoux-Guillaume et al., 2004 and 2018a)* and tectonically deformed grains (*Fougerouse et al., 2021b*), did not display Bragg diffraction contrasts in bright field mode (with their corresponding SAED patterns) as pronounced as those described here that correspond to mosaïcism and deformation bands. Inside the twinned areas it is almost impossible to distinguish contrasts in shocked monazite from those of tectonically deformed monazite, except in the case where twin orientations are specifically characteristic of shock deformation (*Erickson et al., 2016*; *Fougerouse et al., 2021a*). However, in the case of common twin orientations, like those in the present study with (001), this criterion is not sufficient. The diffraction contrasts are also not discriminating, as in the twinned domains neither extra spots nor streaking of spots were observed. In this case the diffraction contrasts observed in BF-TEM can be directly attributed almost entirely to radiation damage and not shock metamorphism. Finally, the assumption that the presence of crystal defects (e.g. dislocations) in naturally shocked monazite samples may indicate that these defects were not annealed after an impact event should be considered along with the observation that radiation damage in monazite is continuously created and healed over geological time.

CONCLUSIONS

This study demonstrated the ability of laser-driven shock experiments using a high-energy laser pulse of ns-order duration to reproduce shock-deformation microstructures observed in natural shocked monazite. We describe three main microstructural features at the nanoscale: deformation twins, mosaïcism, and deformation bands. The deformation twins formed in (001), an orientation that is not diagnostic of shock deformation. However, both mosaïcism and deformation bands, expressed in SAED pattern with streaking of spots, and the presence of extra spots, more or less pronounced, provide evidence to identify shocked monazite grains. Other shock-deformation features reported in naturally shocked monazite, such as high-pressure polymorphs and neoblastic domains, were not observed in the experimental charges. Further study is needed to evaluate the possibility of forming such features with laser-driven shock experiments. Furthermore, as the presence of radiation damage may also modify the formation of shock-deformation features, use of monazite crystals free of radiation damage may help to answer this question.

If Ca segregation along deformation twin boundaries, as revealed in both naturally and experimentally shocked-monazite crystals using TEM, is a consequence of shock-deformation, future studies can similarly evaluate the potential for Pb mobility and the geochronological response to shock events by combining structural and isotopic observations at the nanoscale. *Fougerouse et al. (2021a)* suggested that Pb may be expelled from monazite during shock twin formation, depending on the temperature during the impact event (>900 °C). Work is in progress to see if Pb can be expelled from monazite during such laser-shock experiments, either during twin formation or maybe during formation of these highly disoriented band features, and then reset the U-(Th)-Pb clock.

Acknowledgments

This project has received financial support from the CNRS through the INSU-PNP, the MITI interdisciplinary programs and the IEA Nanomobility. The CLyM (Consortium Lyon St-Etienne de Microscopie) is thanked for access to the TEM NeoARM in Saint-Etienne (France). The Raman facility

in Lyon (France) is supported by the Institut National des Sciences de l'Univers (INSU). It is a contribution of the LABEX Lyon Institute of Origins (ANR-10- LABX-0066), within the program "Investissements d'Avenir" (ANR-11-IDEX-0007) at Université de Lyon. AJC acknowledges funding from the Space Science and Technology Centre at Curtin University. We thank the editor William B. McKinnon and reviewer Axel Wittmann for valuable comments that greatly improved the final version of this manuscript.

References

Cavosie, A.J., Erickson, T.M., Montalvo, P.E., Prado, D.C., Cintron, N.O. and Gibbon, R.J. (2018). The Rietputs Formation in South Africa. In: Microstructural Geochronology (eds D.E. Moser, F. Corfu, J.R. Darling, S.M. Reddy and K. Tait), 203-224. https://doi.org/10.1002/9781119227250.ch9

Cavosie, A.J., Kirkland, C.L., Reddy, S.M., Timms, N.E., Talavera, C., and Pincus, M.R. (2021). Extreme plastic deformation and subsequent Pb loss in shocked xenotime from the Vredefort Dome, South Africa . In Large Meteorite Impacts and Planetary Evolution VI : Geological Society of America Special Paper (eds Reimold, W.U., and Koeberl, C.), 550, 465-478.

Cavosie, A.J., Quintero, R.R., Radovan, H.A., and Moser, D.E. (2010). A record of ancient cataclysm in modern sand: shock microstructures in detrital minerals from the Vaal River, Vredefort Dome, South Africa. Geological Society of America Bulletin, v. 122, p. 1968‑1980.

D'Abzac, F.-X., Seydoux-Guillaume, A.-M., Chmeleff, J., Datas, L., Poitrasson, F. (2012) In situ characterization of infrared femtosecond laser ablation in geological samples. Part A: the laser induced damage. Journal of Analytical Atomic Spectrometry 27, 99–107.

Du, A., Wan, C., Qu, Z. and Pan, W. (2009). Thermal conductivity of monazite-type $REPO_4$ (RE=La, Ce, Nd, Sm, Eu, Gd). Journal of the American Ceramic Society, 92, 2687-2692. https://doi.org/10.1111/j.1551-2916.2009.03244.x

Erickson, T.M., Kirkland, C.L., Timms, N.E., Cavosie, A.J. and Davison, T.M. (2020) Precise radiometric age establishes Yarrabubba, Western Australia, as Earth's oldest recognized meteorite impact structure. Nature Communication 11(1), 1-8.

Erickson, T.M., Timms, N.E., Kirkland, C.L., Tohver, E., Cavosie, A.J., Pearce, M.A. and Reddy, S.M. (2017) Shocked monazite chronometry: integrating microstructural and in situ isotopic age data for determining precise impact ages. Contribution to Mineralogy and Petrology 172(2-3), 11.

Erickson, T.M., Timms, N.E., Pearce, M.A., Cayron, C., Deutsch, A., Keller, L.P. and Kring, D.A. (2019) Shock-produced high pressure (La, Ce, Th) PO_4 polymorph revealed by microstructural phase heritage of monazite. Geology 47(6), 504-508.

Erickson, T.M., Cavosie, A.J., Moser, D.E., Barker, I.R., Radovan, H.A., and 499 Wooden, J. (2013). Identification and provenance determination of distally transported, Vredefort-derived shocked minerals in the Vaal River, South Africa using SEM and SHRIMP-RG techniques. Geochimica et Cosmochimica Acta, 107, 170-188.

Erickson, T.M., Cavosie, A.J., Pearce, M.A., Timms, N.E., Reddy, S.M. (2016). Empirical constraints of shock features in monazite using shocked zircon inclusions. Geology, 44, 635-638.

Erickson, T.M., Pearce, M.A., Taylor, R.J.M., Timms, N.E., Clark, C., Reddy, S.M., and Buick, I.S. (2015) Deformed monazite yields high-temperature tectonic ages. Geology, 43, 383–386, https://doi.org/10.1130/G36533.1.

Ewing, R.C., Meldrum, A., Wang, L.M., Weber, W.J., Corrales, L.R. (2003). Radiation damage in zircon. In: Hanchar, J.M., Hoskin, P.W.O. (Eds.), Zircon. Reviews in Mineralogy and Geochemistry, vol.53. Mineralogical Society of America, pp.387–425.

Feng, J., Xiao, B., Zhou, R., and Pan, W. (2013). Anisotropy in elasticity and thermal conductivity of monazite-type REPO4 (RE=La, Ce, Nd, Sm, Eu and Gd) from first-principles calculations. Acta Materialia, 61, 19, 7364-7383. 10.1016/j.actamat.2013.08.043.

Fougerouse, D., Cavosie, A., Erickson, T., Reddy, S., Cox, M., Saxey, D., Rickard, W., Michael, T. and Wingate, M. (2021a). A new method for dating impact events – Thermal dependency on nanoscale

566 Pb mobility in monazite shock twins. Geochim. Cosmochim. Acta, 314, 381-396.
567 https://doi.org/10.1016/j.gca.2021.08.025
568 Fougerouse, D., Reddy, S.M., Seydoux-Guillaume, A.-M, Kirkland, C.L., Erickson, T.M., Saxey, D.W.,
569 Rickard, W.D.A., Jacob, D., Leroux, H., and Clark, C. (2021b). Mechanical twinning of monazite
570 expels radiogenic Pb. Geology, 49, 417-421. https://doi.org/10.1130/G48400.1
571 Fougerouse, D., Reddy, S.M., Saxey, D.W., Erickson, T., Kirkland, C.L., Rickard, W.D.A., Seydoux-
572 Guillaume, A.-M., Clark, C., and Buick, I.S. (2018). Nanoscale distribution of Pb in monazite revealed
573 by atom probe microscopy. Chemical Geology, 479, 251-258.
574 https://doi.org/10.1016/j.chemgeo.2018.01.020
575 French, B.M. and Koeberl, C. (2010) The convincing identification of terrestrial meteorite impact
576 structures: what works, what doesn't, and why. Earth Science Review 98(1-2), 123-170.
577 Gardès, E., Montel, J.-M., Seydoux-Guillaume, A.M., and Wirth, R. (2007). Pb diffusion in monazite:
578 New constraints from the experimental study of Pb^{2+} <=> Ca^{2+} Geochimica et Cosmochimimica
579 Acta, 71, 4036-4043.
580 Gouadec, G., and Colomban, P. (2007). Raman Spectroscopy of nanomaterials: How spectra relate to
581 disorder, particle size and mechanical properties. Progress in Crystal Growth and Characterization
582 of Materials 53, 1-56
583 Grand'Homme, A., Janots, E., Seydoux-Guillaume, A.-M., Guillaume, D., Magnin, V., Hövelmann, J.,
584 Höschen, C., and Boiron, M.C. (2018). Mass transport and fractionation during monazite alteration
585 by anisotropic replacement. Chemical Geology, 484, 51-68.
586 Hay, R.S., and Marshall, D.B. (2003) Deformation twinning in monazite. Acta Materialia, 51, 5235-5254.
587 Heuser, J.M., Palomares, R.I., Bauer, J.D., Lozano Rodriguez, M.J., Cooper, J., Lang, M., Scheinost, A.C.,
588 Schlenz, H., Winkler, B., Bosbach, D., Neumeier, S., Deissmann, G. (2018). Structural
589 characterization of (Sm,Tb)PO4 solid solutions and pressure-induced phase transitions. Journal of
590 the European Ceramic Society, 38, 11, 4070-4081.

591 Huang, T., Lee, J.-S., Kung, J., and Lin, C.-M. (2010). Study of monazite under high pressure. Solid State
592 Communications, v. 150, p. 1845–1850, https:// doi .org /10 .1016 /j .ssc .2010 .06 .042 .
593 Jourdan, F., Reimold, W. U. and Deutsch, A. (2012) Dating terrestrial impact structures. Elements 8(1),
594 49-53.
595 Lacomba-Perales, R., Errandonea, D., Meng, Y., and Bettinelli, M. (2010). High-pressure stability and
596 compressibility of *A*PO4 (*A* = La, Nd, Eu, Gd, Er, and Y) orthophosphates: An X-ray diffraction study
597 using synchrotron radiation. Physical Review B: Condensed Matter and Materials Physics, 81,
598 064113, https:// doi .org /10 .1103 /PhysRevB .81 .064113.
599 Lang, M., Zhang, F., Lian, J., Trautmann, C., Neumann, R., Ewing, R.C. (2008). Irradiation-induced
600 stabilization of zircon (ZrSiO4) at high pressure. Earth and Planetary Science Letters, 269, 291-295.
601 doi:10.1016/j.epsl.2008.02.027
602 Langenhorst, F., Boustie, M., Migault, A., Romain, J.P. (1999) Laser shock experiments with
603 nanoseconds pulses: a new tool for the reproduction of shock defects in olivine. Earth and
604 Planetary Science Letters 173, 333-342.
605 Langenhorst, F. and Deutsch, A. (2012) Shock metamorphism of minerals. Elements 8(1), 31–36.
606 Leroux, H. (2001). Microstructural shock signatures of major minerals in meteorites. *European Journal*
607 *of Mineralogy* 13, 253–272.
608 Leroux, H., Reimold, W., Koeberl, C., Hornemann, U. and Doukhan, J.-C. (1999) Experimental shock
609 deformation in zircon: a transmission electron microscopic study. Earth Planet. Sci. Lett. 169(3–4),
610 291–301.
611 Leroux, H., Reimold, W.U., and Doukhan, J.-C. (1994). A TEM investigation of shock metamorphism in
612 quartz from the Vredefort dome, South Africa, Tectonophysics, 230, 223-239.
613 https://doi.org/10.1016/0040-1951(94)90137-6.
614 Moser, D.E., Arcuri, G.A., Reinhard, D.A., White, L.F., Darling, J.R., Barker, I.R., Larson, D.J., Irving, A.J.,
615 McCubbin, F.M., Tait, K.T., Roszjar, J., Wittmann, A. and Davis, C. (2019). Decline of giant impacts

616 on Mars by 4.48 billion years ago and an early opportunity for habitability. Nature Geoscience, 12,
617 522-527.
618 Nasdala, L., Wenzel, M., Vavra, G., Irmer, G., Wenzel, T., and Kober, B. (2001) Metamictisation of
619 natural zircon: accumulation versus thermal annealing of radioactivity-induced damage. Contrib.
620 Mineralogy and Petrology, 141, 125-144.
621 Nasdala, L., Lengauer, C.L., Hanchar, J.M., Kronz, A., Wirth R., Blanc, P., Kennedy, A.K., Seydoux-
622 Guillaume, A.M. (2002). Annealing radiation damage and the recovery of cathodoluminescence.
623 Chemical Geology, 191, 121-140.
624 Ni, Y., Hughes, J.M., and Mariano, A.N. (1995). Crystal chemistry of the monazite and xenotime struc-
625 tures. American Mineralogist, 80, 21-26, https://doi.org/10.2138/am-1995-1-203.
626 Paquette, J.L., and Tiepolo, M., 2007. High resolution (5 µm) U–Th–Pb isotope dating of monazite with
627 excimer laser ablation (ELA)-ICPMS. Chemical Geology 240, 222-237.
628 Peterman, E.M., Reddy, S.M., Saxey, D. W., Snoeyenbos, D.R., Rickard, W.D., Fougerouse, D. and
629 Kylander-Clark, A.R. (2016). Nanogeochronology of discordant zircon measured by atom probe
630 microscopy of Pb-enriched dislocation loops. Science Advance 2(9) e1601318.
631 Reimold, W.U., Leroux, H. and Gibson, R.L. (2002) Shocked and thermally metamorphosed zircon from
632 the Vredefort impact structure, South Africa: a transmission electron microscopic study. Eur. J.
633 Mineral. 14, 859-868.
634 Ruschel, K., Nasdala, L., Kronz, A., Többens D.M., Škoda R., Finger F., and Möller A. (2012). A Raman
635 spectroscopic study on the structural disorder of monazite–(Ce). Mineralogy and Petrology 105,
636 41-55. https://doi.org/10.1007/s00710-012-0197-7
637 Schmieder, M. and Kring, D.A. (2020) Earth's impact events through geologic time: a list of
638 recommended ages for terrestrial impact structures and deposits. Astrobiology 20(1), 91–141.
639 Seydoux-Guillaume, A.-M., Bingen, B., Bosse, V., Janots, E. and Laurent, A.T. (2018a). Transmission
640 Electron Microscope imaging sharpens geochronological interpretation of zircon and monazite. In:

641 Microstructural Geochronology (eds D.E. Moser, F. Corfu, J.R. Darling, S.M. Reddy and K. Tait), 261-
642 275. https://doi.org/10.1002/9781119227250.ch12
643 Seydoux-Guillaume, A.-M., Deschanels, X., Baumier, C., Neumeier, S., Weber, W.J., and Peuget, S.
644 (2018b). Why natural monazite never becomes amorphous: experimental evidence for alpha self-
645 healing. American Mineralogist, 103, 824-827. doi.org/10.2138/am-2018-6447
646 Seydoux-Guillaume, A.-M., Fougerouse, D., Laurent, A.T., Gardes, E., Reddy, S.M., Saxey, D.W. (2019).
647 Nanoscale resetting of the Th/Pb system in an isotopically-closed monazite grain: a combined Atom
648 Probe and Transmission Electron Microscopy study. Geoscience Frontiers, 10, 65-76.
649 https://doi.org/10.1016/j.gsf.2018.09.004.
650 Seydoux-Guillaume, A.-M., Freydier., R., Poitrasson, F., D'Abzac, F.-X., Wirth, R., Datas, L. (2010)
651 Dominance of mechanical over thermally induced damage during femtosecond laser ablation of
652 monazite. European Journal of Mineralogy 22, 235-244.
653 Seydoux-Guillaume, A.-M., Goncalves, P., Wirth, R. and Deutsch, A. (2003). TEM study of polyphasic
654 and discordant monazites: site specific specimen preparation using the Focused Ion Beam
655 technique. Geology, 31, 973-976.
656 Seydoux-Guillaume, A.-M., Wirth, R., Deutsch, A., and Schärer, U. (2004). Microstructure of 24-1928
657 Ma concordant monazites: implications for geochronology and nuclear waste deposits. Geochimica
658 et Cosmochimica Acta, 68, 2517-2527.
659 Seydoux-Guillaume, A.-M., Wirth, R., Nasdala, L., Gottschalk, M., Montel, J.-M. and Heinrich, W.
660 (2002). An XRD, TEM and Raman study of experimentally annealed natural monazite. Physics and
661 Chemistry of Minerals, 29, 240-253.
662 Timms, N.E., Erickson, T.M., Pearce, M.A., Cavosie, A.J., Schmieder, M., Tohver, E., Reddy, S.M.,
663 Zanetti, M.R., Nemchin, A.A. and Wittmann, A. (2017) A pressure-temperature phase diagram for
664 zircon at extreme conditions. Earth-Sci. Rev. 165, 185–202.
665 Timms, N.E., Healy, D., Erickson, T.M., Nemchin, A.A., Pearce, M.A. and Cavosie, A.J. (2018). Role of
666 Elastic Anisotropy in the Development of Deformation Microstructures in Zircon. In Microstructural

667 Geochronology (eds D.E. Moser, F. Corfu, J.R. Darling, S.M. Reddy and K. Tait).
668 https://doi.org/10.1002/9781119227250.ch8.
669 Wittmann, A., Kenkmann, T., Schmitt, R.T., and Stöffler, D. (2006) Shock-metamorphosed zircon in
670 terrestrial impact craters. Meteoritics & Planetary Science, 41, 433-454, doi:10.1111 /j.1945-
671 5100.2006.tb00472.x.
672
673 **Figure captions**
674 **Figure 1** - Monazite single crystal before and after shock experiment. a-d. Optical views (a-c: binocular
675 and d: reflected light) from the 3 mm shocked area (central zone). e-g: Secondary Electron Microscope
676 images from 2 areas in the central zone where characterizations were performed. Arrows point to
677 cracks induced by shock.
678 **Figure 2** – Raman spectra performed in unshocked and shocked (C1 and C2) domains from monazite
679 crystal. a- average and standard deviation of the Raman spectra per group. b- diagram showing the
680 FWHM (full width at half maximum) of the v1 peak as a function of its spectral position (in cm^{-1}). These
681 values were corrected for the apparatus function of the Raman instrument (*Nasdala et al. 2001*). The
682 peak positions and FWHM were determined without smoothing spectra and a linear baseline was used
683 in the spectral range 800-1200 cm^{-1}. The reproducibility is better than +/- 0.01 cm^{-1} and our
684 uncertainties on data are two magnitude lower than 1 cm^{-1}.
685 **Figure 3** – Bright Field Transmission Electron Microscope (BF-TEM) images (a-b and d) and Selected
686 Area Electron Diffraction (SAED – c and e) from FIB-foil (FIB5) prepared from C2 area - Mosaïcism.
687 Note mottled diffraction contrasts (a-b), streaking of diffraction spots (c), moiré fringes (arrows in d),
688 and extra spots in [100] oriented SAED (arrows in e), characteristic features from mosaïcism
689 (misoriented subgrains).
690 **Figure 4** – Bright Field Transmission Electron Microscope (BF-TEM) images (a-d) and Selected Area
691 Electron Diffraction (SAED - e) from FIB-foil (FIB5) prepared from C2 area - Highly-disoriented bands.

Note the presence of band features almost parallel to each other (a and b), in a domain that is deeper in the FIB foil (a). Note a very reduced crystallinity inside these bands, with almost no Bragg contrasts (homogeneous grey – c and d). SAED pattern (e) realized across one band and the monazite (inset in d) in zone axis [100], shows streaking of some spots and a lot of extra spots (arrows in e) proof for highly disoriented domains.

Figure 5 – Annular Dark Field Scanning TEM (STEM) images from FIB-foil (FIB5) prepared from C2 area in the highly-deformed bands domain. a- Low magnification ADF-STEM image showing the presence of bands domains appearing darker (less diffracting regions). b- zoom in one band domain. c- Zoom in area inset in b and three Fast Fourier Transform (FFT) from different domains in c showing contrasts between the bright perfectly ordered domain (FFT1) and dark highly disoriented (FFT2 and 3) domains (bands). Note arrow indicating extra spot in FFT2 (measured at 3.2 Å). d-e: zoom from image in c. Note the crystallographic fringes still visible in the dark band domain (d and e). The perfectly ordered ADF-STEM image in f shows arrangements of heavy atoms in [100] zone axis, in agreement with the crystallographic model (see Supp data S2).

Figure 6 – Bright (a-d) and Dark Field (f) Transmission Electron Microscope (BF/DF-TEM) images, and Selected Area Electron Diffraction (SAED – e and g) from FIB-foil (FIB1) prepared in C1 area - Twinned domain. a-c BF-TEM showing twins almost horizontal in the images. Note the presence of mottled diffraction contrasts however much less pronounced than in other areas described in figures 3 and 4. e- SAED pattern in one twin (inset in a) along [110] zone axis. Note the absence of streaking of spots nor extra spots. f- DF-TEM of a twin with (11-1) diffraction spot. g- SAED pattern realized across one twin boundary showing their (001) directions.

Figure 7 – High Resolution STEM images from FIB-foil (FIB1) prepared from C1 area. Annular Dark Field (a) and Annular Bright Field (b) STEM images across the same twin boundary in (001) with high magnification image (c) in ADF mode from left part of the twin in zone axis [110]. Note only the heavy atoms can be observed with this detector and their arrangements in [110] fit the crystallographic

model ($CePO_4$). Ca(Kα) distribution in the same area as in a and b with enrichment within the twin boundary (d). Details in Supp. Data S2.

Figure 8 - Bright Field TEM images (a-c), SAED patterns (d-f), and High Resolution ADF-STEM images (g-i) from two FIB-foils prepared in two different areas from one naturally shocked monazite grain (Mnz9) from Rietputs formation (South-Africa; *Cavosie et al., 2018*). Three kinds of deformation features are seen: twins (a, d, g and h) in (001) with Ca enrichment within the boundary (Ca map from inset in h), mosaïcism (b and e) and highly deformed band-features (c, f and i). Note streaking of spots (e and f), extra spots in SAED patterns (indicated by arrows, with d_{hkl} of 3.25 Å and 3.26 Å for e and f respectively). Details on location of FIB foils and on chemical mapping are given in Supp. Data S2.

Figures

Figure 1:

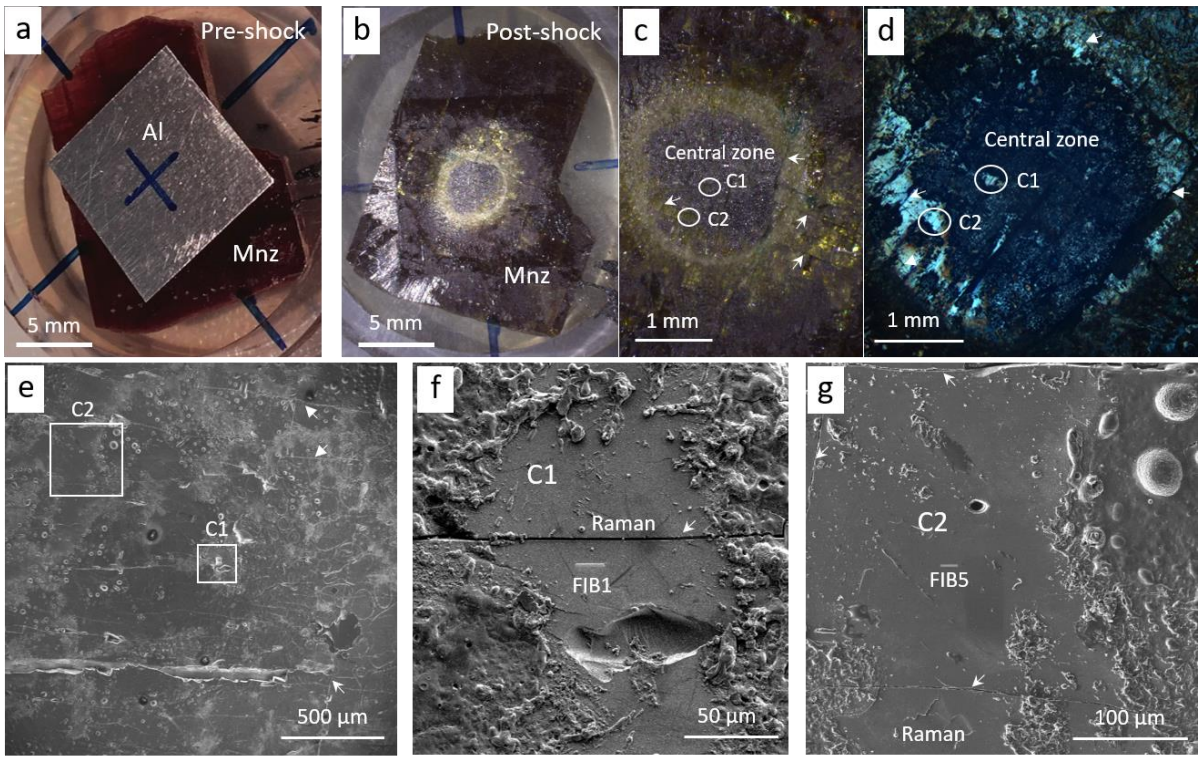

Figure 2:

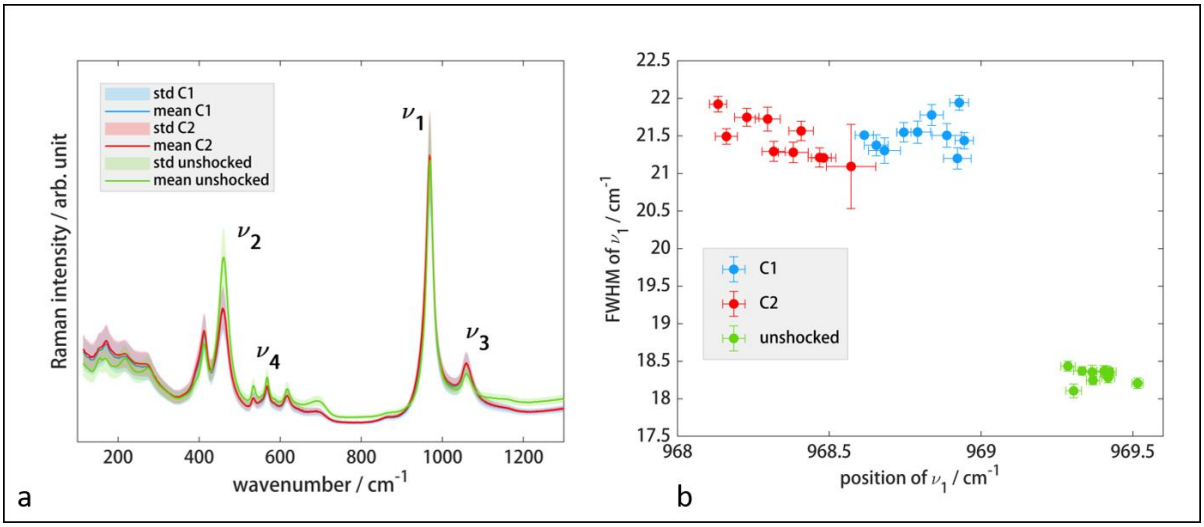

730

731 **Figure 3:**

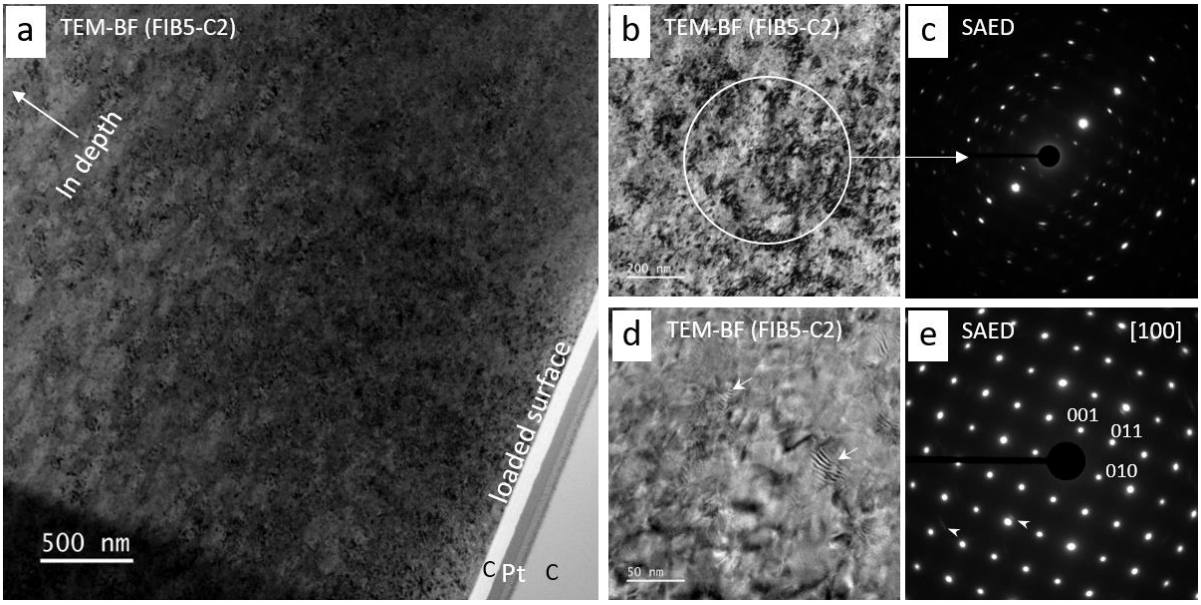

732

733 **Figure 4:**

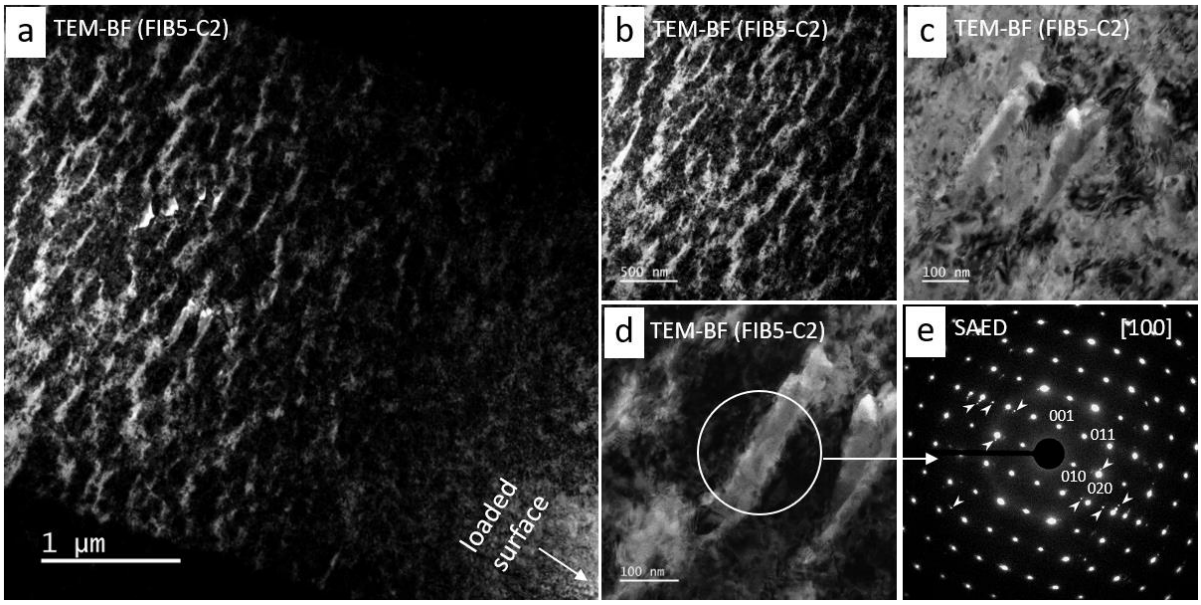

734

735 **Figure 5:**

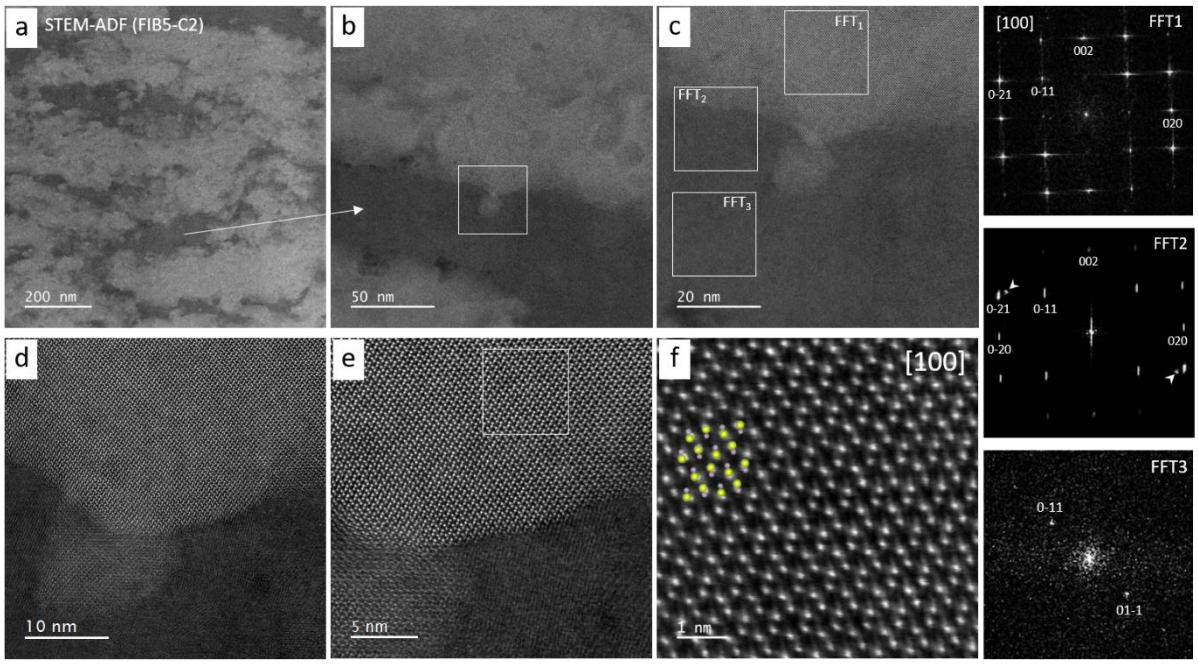

736

737 **Figure 6:**

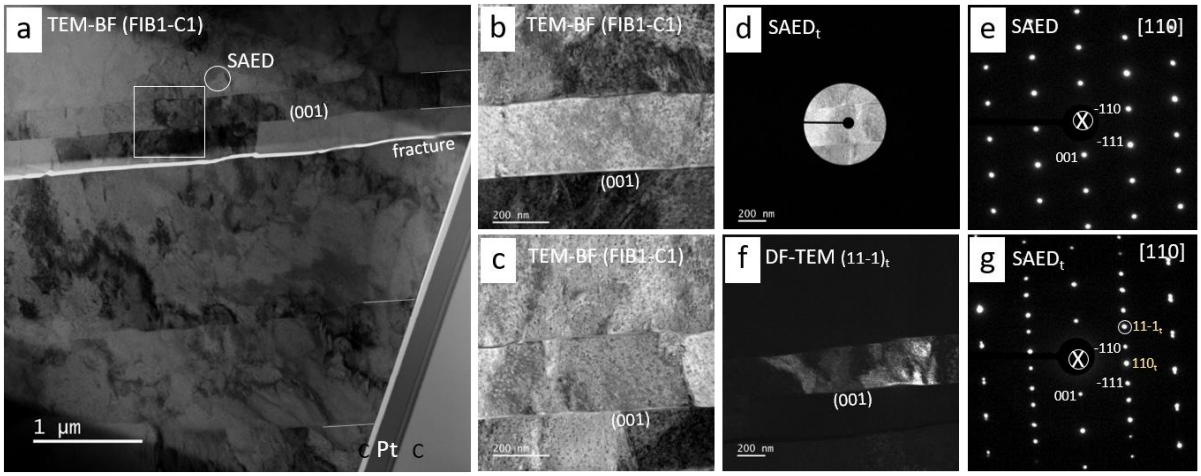

738

739 **Figure 7:**

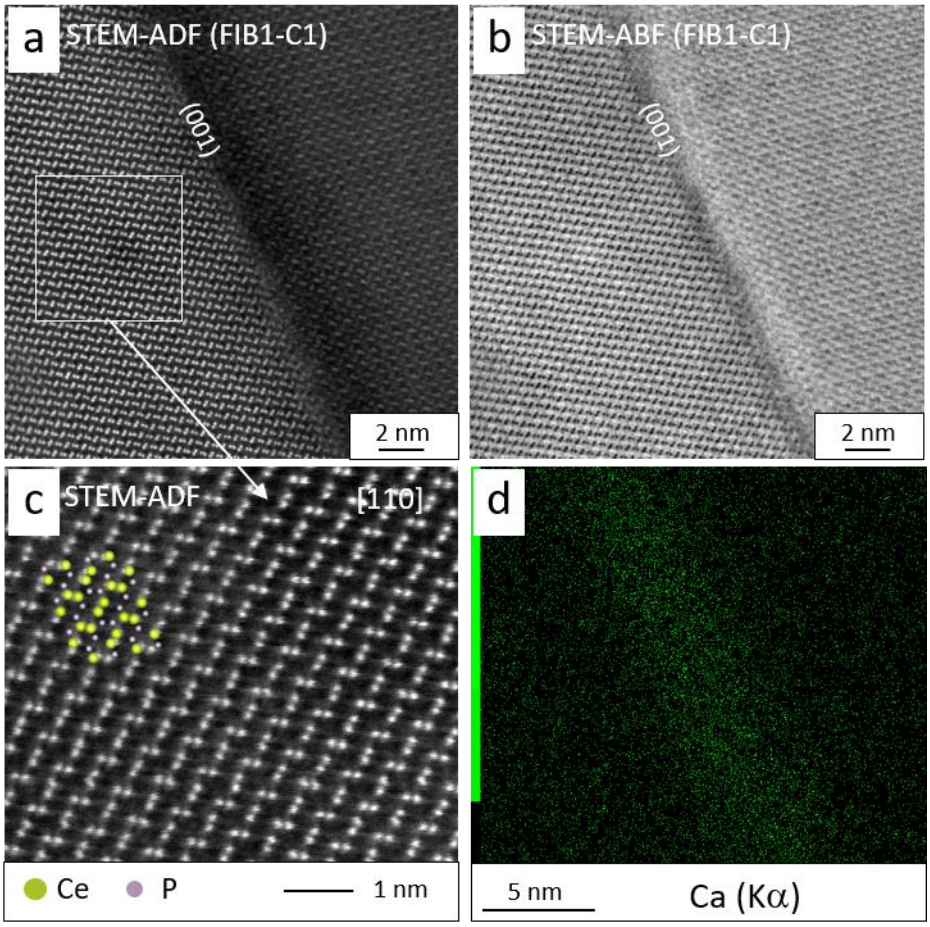

740

741 **Figure 8:**

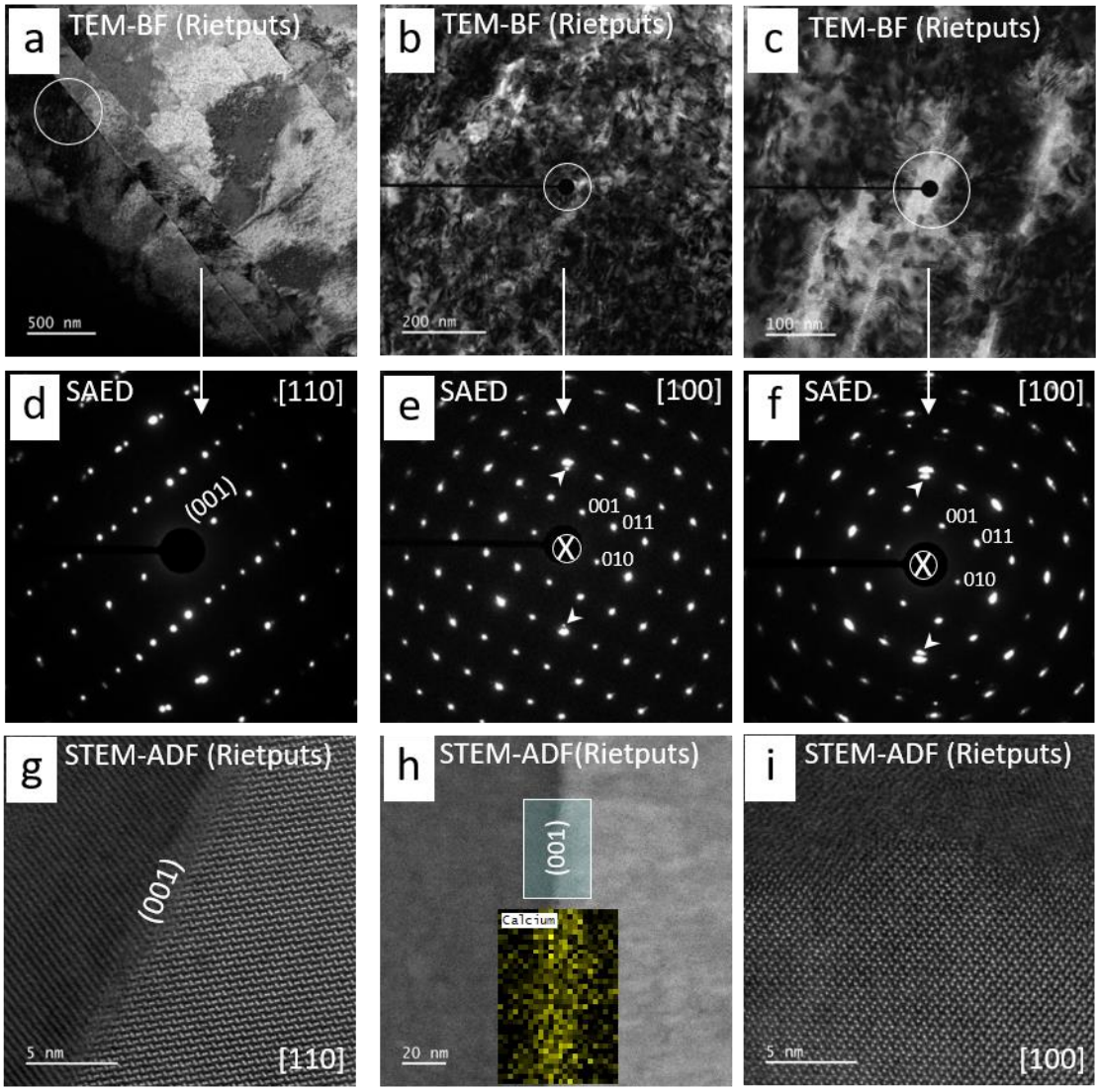
a
TEM-BF (Rietputs)
500 nm
b
TEM-BF (Rietputs)
200 nm
c
TEM-BF (Rietputs)
100 nm
d
SAED
[110]
(001)
e
SAED
[100]
001
011
010
f
SAED
[100]
001
011
010
g
STEM-ADF (Rietputs)
(001)
5 nm
[110]
h
STEM-ADF(Rietputs)
(001)
Calcium
20 nm
i
STEM-ADF (Rietputs)
5 nm
[100]

742

743